LANGMUIR

pubs.acs.org/Langmuir Article

Liquid Heterostructures: Generation of Liquid–Liquid Interfaces in Free-Flowing Liquid Sheets

David J. Hoffman, Hans A. Bechtel, Diego A. Huyke, Juan G. Santiago, Daniel P. DePonte, and Jake D. Koralek*

Cite This: *Langmuir* 2022, 38, 12822–12832 Read Online

ACCESS | Metrics & More | Article Recommendations | Supporting Information

ABSTRACT: Chemical reactions and biological processes are frequently governed by the structure and dynamics of the interface between two liquid phases, but these interfaces are often difficult to study due to the relative abundance of the bulk liquids. Here, we demonstrate a method for generating multilayer thin film stacks of liquids, which we call liquid heterostructures. These free-flowing layered liquid sheets are produced with a microfluidic nozzle that impinges two converging jets of one liquid onto opposite sides of a third jet of another liquid. The resulting sheet consists of two layers of the first liquid enveloping an inner layer of the second liquid. Infrared microscopy, white light reflectivity, and imaging ellipsometry measurements demonstrate that the buried liquid layer has a tunable thickness and displays well-defined liquid–liquid interfaces and that this inner layer can be only tens of nanometers thick. The demonstrated multilayer liquid sheets minimize the amount of bulk liquid relative to their buried interfaces, which makes them ideal targets for spectroscopy and scattering experiments.

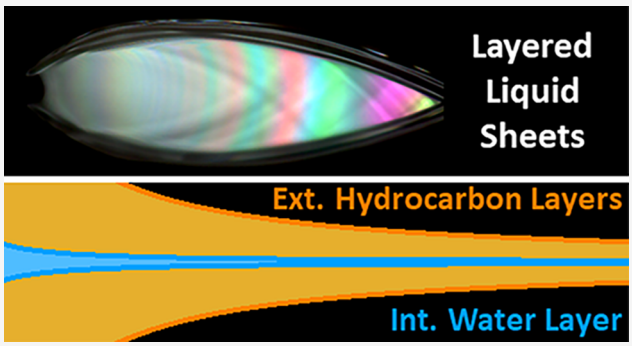

INTRODUCTION

Liquid–liquid interfaces are of key importance to biology, chemistry, and engineering. These interfaces can be the sites of reactions,[1] adsorption,[2] self-assembly,[3] and chemical or electron transfer.[4] Despite its significance, the liquid–liquid interface and its vicinity remains difficult to study as the interface contains far fewer molecules than the bulk in typical systems. This asymmetry makes isolating spectroscopic or scattering signals from the interface challenging, and has inspired many surface-specific or surface-enhanced spectroscopies.[5,6] The liquid–liquid interface could be better examined by minimizing the amount of liquid not comprising the interface, effectively minimizing the bulk signal, which could enable the investigation of interfaces with non-specialized techniques.

Toward the goal of generating efficient targets for liquid–liquid interface studies, the present work demonstrates the generation of liquid heterostructures: liquid sheet jets comprising thin, discrete layers of different liquids. Microfluidic liquid jets, and, in particular, sheet jets,[7−13] have been rapidly gaining popularity for liquid-phase spectroscopic experiments. These liquid sheet jets are flat, vacuum-stable, fast-flowing, free-standing laminar liquid structures that can have sub-micron thicknesses. Additionally, the sheets are rapidly self-refreshing, thus avoiding accumulated sample or container damage from high-intensity or ionizing radiation. These qualities have led to their adoption for extreme ultraviolet/soft X-ray spectroscopies,[7,9] ultrafast electron diffraction,[14,15] and a range of other uses, such as high-harmonic generation and high-intensity laser targets.[16−18] Conventional microfluidics studies have also demonstrated that well-defined liquid–liquid interfaces can form between immiscible fluids in laminar flow,[19,20] suggesting that liquid sheet jets may provide a general platform for studying liquid–liquid interfaces.

The liquid heterostructures demonstrated here were produced by impinging a cylindrical liquid jet with two flanking cylindrical jets of a second, immiscible liquid. This flow occurs inside a three-channel microfluidic nozzle, with the three microfluidic channels intersecting at the nozzle exit. When liquid flows through the outer channels at sufficiently high flow rates, Q_{out}, the collision of the jets generates a leaf-shaped liquid sheet bounded by a thicker, cylindrical rim. The sheet is orthogonal to the plane of the original colliding jets (illustrated in Figure 1) as the momentum of the colliding jets drives the liquid radially outward from the collision point.[21−24] Surface tension gradually brings the cylindrical rims back

Received: June 30, 2022
Revised: September 21, 2022
Published: October 11, 2022

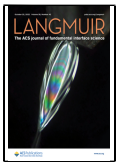

https://doi.org/10.1021/acs.langmuir.2c01724
Langmuir 2022, 38, 12822–12832

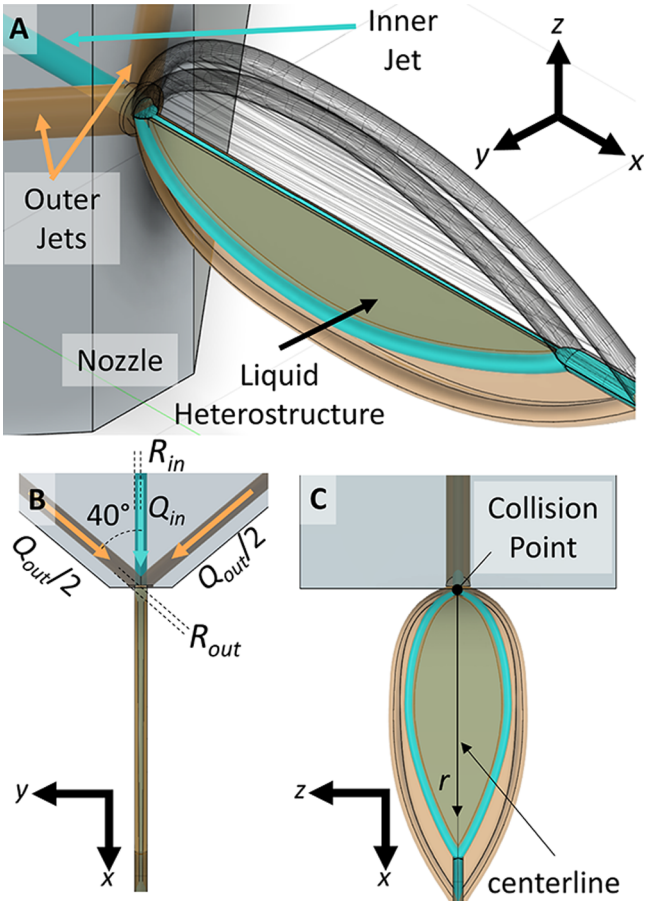

Figure 1. (A) Schematic cross-sectional diagram of the microfluidic nozzle and liquid heterostructure sheet jet. The three cylindrical jets (in the *XY* plane) meet at the end of the nozzle, where the hydrodynamic forces from the impinging outer jets (orange) generate a sheet in the *XZ* plane. The inner jet of an immiscible fluid (cyan) is flattened into a discrete layer within the sheet. The cyan rim of the sheet is thinly coated by the outer orange fluid but is highlighted cyan for clarity. (B) Side view of the sheet, illustrating the geometry of the microfluidic nozzle. (C) Top view of the sheet indicating *r*: the distance from the collision point at the nozzle exit along the sheet's centerline.

together to form the node at the downstream end of the sheet. The inner jet of the second liquid is flattened into a thin layer by the same hydrodynamic forces that generate the outer sheet while also being completely enveloped in the outer sheet. This process is analogous to the generation of a gas-accelerated liquid sheet jet from a cylindrical jet using the same type of microfluidic nozzle,[11] except with a second liquid replacing the pressurized gas.

The produced heterostructure dimensions were found to depend on flow rates and liquid properties. The thicknesses of the liquid layers were measured with Fourier transform infrared (FTIR) microscopy, which provides spatially resolved absorption spectra that can be used to determine the total quantity of each liquid at each point in the sheet. The inner layer thickness was found to be tunable from >1 μm to <100 nm by adjusting relative flow rates and followed similar scaling relations as the outer layers. The existence of distinct buried interfaces within the liquid sheet was then confirmed using reflectivity and imaging ellipsometry measurements. The buried interfaces provide additional surfaces for incident light to reflect from and thus generate thin film interference effects. As the sheet layers vary in thickness with the distance from the nozzle, the additional reflections manifest as intensity modulations in the sheet's thin film interference pattern. The reflection intensity modulations result in corresponding phase and polarization modulation in the ellipsometry measurements. These measurements were compared to the predicted ellipsometric observables and white light reflection from an ideal heterostructure with layer thicknesses determined from FTIR measurements and showed excellent agreement. The results indicate that the buried interfaces are sufficiently sharp and smooth to produce coherent optical reflections, indicating a high-quality liquid heterostructure.

EXPERIMENTAL MATERIALS AND METHODS

Microfluidic Chip and Sheet Jet Operation. The microfluidic sheet nozzle was a custom design (shown in the Supporting Information) manufactured by Micronit Microtechnologies BV using standard lithographic techniques. The geometry of the chip can be seen in Figure 1. The chip nozzles used for this study had outer channels (R_{out} = 20 μm), which meet an inner channel (R_{in} = 10 μm) at ±40°. The three channels meet at a distance of 25 μm from the exit of the nozzle, where the liquid jets collide. These convergent flows in the lithographically defined channels produce similar flows to colliding jets in air.

Liquids were supplied to the microfluidic chip channels using two HPLC pumps (Shimadzu) connected to pulsation dampeners. The pulsation dampeners were homebuilt and consisted of ∼1 mL of steel tubing held vertically and connected by a tee joint to the HPLC output. The dampener traps an air bubble, which serves as a spring to dampen any pressure fluctuations. The outer channels were supplied with one liquid at a combined flow rate, Q_{out}, ranging from 1.5 to 2.0 mL/min, while the inner channel was supplied a second liquid at a flow rate, Q_{in}, ranging up to 600 μL/min. The immiscible liquid pairs of water (Wat)/toluene (Tol) and water/cyclohexane (Cy) were chosen for the relatively high indices of refraction of toluene and cyclohexane[25] in visible wavelengths in comparison to water,[26] which enables the reflectometry and ellipsometry experiments discussed below.

FTIR Spectromicroscopy. The liquid heterostructures were imaged at beamline 2.4 at the Advanced Light Source using an Agilent Cary 620 FTIR microscope working at 5.5 μm spatial resolution. The FTIR microscope fitted with a 15× all-reflective objective (NA = 0.62) and a 128 × 128 MCT pixel-array detector. For these measurements, a globar source and KBr beamsplitter were employed. The FTIR spectrometer and microscope were purged with nitrogen, except for the space between the objectives. The liquid sheets were operated in air in a custom sample cell with 1 mm-thick CaF_2 windows connected to a 1/4″ vacuum drain hose. For some fluids and flow rates, the sheets were found to be thick enough at points to produce noticeable thin film interference at infrared wavelengths (2.5−10 μm), which produced an oscillatory spectral background. This background was modeled and subtracted using the transfer matrix method (see the Supporting Information).[27,28]

The IR absorption spectra could be used to determine the layer thicknesses in the heterostructure through a straightforward application of Beer's law:

$$A(\omega) = \varepsilon(\omega)cl \quad (1)$$

where A is the absorption at frequency ω, ε is the molar absorptivity of the relevant species at that frequency, c is the concentration of the species, and l is the optical path length. As the liquid combinations used are essentially insoluble (with saturated solutions at room temperature of <0.1% w/w for all cases), the concentrations are effectively the same as for neat solvents (55.5 M for water, 9.4 M for toluene, and 9.3 M for cyclohexane). With knowledge of the relevant molar absorptivities, the layer thicknesses of a given heterostructure can be readily determined from the measured absorbances. For this

https://doi.org/10.1021/acs.langmuir.2c01724
Langmuir 2022, 38, 12822−12832

work, the integrated intensities of the absorbance peaks were considered to improve the signal-to-noise ratio.

Microscopy and Imaging Ellipsometry. The reflection microscopy images were taken with a color CMOS camera (Motic, Moticam 2.0) through a 10× long working distance objective (NA 0.28). White light images used white LEDs (Thorlabs LIUCWHA) at a 15° angle of incidence for illumination. Monochromatic reflection microscopy used a 630 nm LED bank source (Thorlabs LIU630A) at indicated angles of incidence. The nozzle was aligned to flow vertically downward for all measurements. The liquid sheet was rotated along its long axis (x in Figure 1) until a specular reflection was observed.

Ellipsometry has been widely employed in the characterization of thin films.[29] The technique leverages differences in the reflectivity of different polarizations of light to gain information on the thickness, roughness, and dielectric properties of thin films. The ellipsometry technique measures the complex reflectance ratio $\rho = r_p/r_s$, where r_p and r_s are the complex-valued reflectivities of p-polarized (in plane of incidence) and s-polarized (perpendicular to plane of incidence) light. This quantity is typically expressed in terms of two ellipsometric angles as

$$\rho = \exp(i\Delta)\tan\Psi \tag{2}$$

where Δ is the phase difference between the reflected polarization components and Ψ relates to the ratio of the s and p reflection amplitudes. Both measured ellipsometric angles are dependent upon the angle of incidence (AOI), θ, of the light source. As ρ is a ratio of reflectivities, the ellipsometric measurements do not require the careful intensity normalizations that are required for quantitative reflectometry measurements. By combining ellipsometric methods with microscopy, it is possible to examine variations in the ellipsometric angles Δ and Ψ across a surface.[30,31] We employed a homebuilt angle-resolved polarization-modulation imaging ellipsometer based on a literature design,[31] which is detailed further in the Supporting Information.

The ellipsometer used the same CMOS camera and 10× long working distance objective (NA 0.28). The 630 nm LED bank source generates light that passes through a linear polarizer set at 45°. The linearly polarized light reflects off the sheet with a different amplitude and phase for the reflected s and p components, depending on the angle of incidence and composition of the sheet. The reflection passes through the objective and through a quarter-wave plate on a motorized rotation stage followed by a linear polarizer set at 90°. By collecting images of the sheet at five quarter-wave plate angles, it is possible to determine both ellipsometric angles at each point of the sheet in the focal plane (see the Supporting Information).

RESULTS

Generating the Liquid Heterostructures. The liquid heterostructures were generated with the same borosilicate microfluidic chip nozzles that have been previously reported to generate ultrathin gas-accelerated liquid sheets.[11] The microfluidic chip is shown schematically in Figure 1 and described in the Experimental Materials and Methods section. The sheet morphology as a function of flow rate was monitored with white light microscopy (see the Experimental Materials and Methods section). For the reflection of white light from thin films, layers of different thicknesses will produce different colored bands due to the constructive or destructive interference at various wavelengths, as discussed in the following sections.

When flow is provided only to the two outer channels, this microfluidic chip forms a single-liquid sheet from the collision of two cylindrical jets (e.g., Figure 2, top). As the collision causes the liquid to expand radially outward at roughly constant velocity, the liquid sheet thickness, h_{out}, created by the collision of two cylindrical jets can be shown to have the approximate form:[21−24]

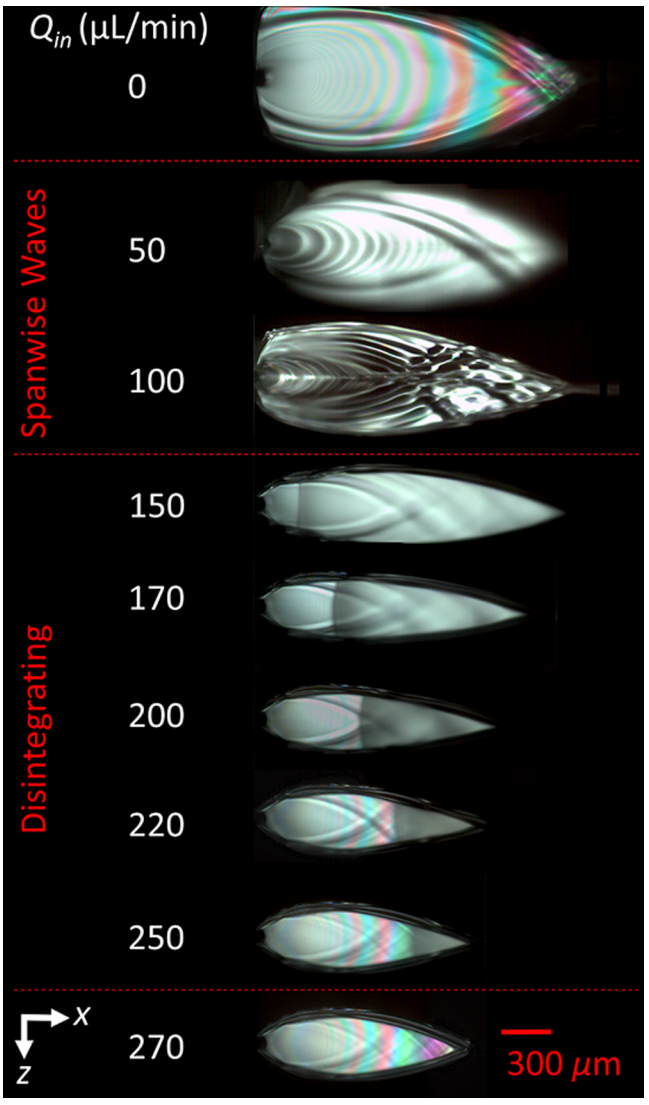

Figure 2. Unstable to stable transition for Tol/Wat/Tol heterostructures (Q_{out} = 1750 μL/min). A pure toluene sheet is shown at the top, and a stable Tol/Wat/Tol heterostructure is shown at the bottom. Intermediate inner liquid flow rates produce unstable structures. The sheets in the "Disintegrating" region transition from stable to unstable midway through the sheet, possibly creating an emulsion within the sheet. Analogous images for Cy/Wat/Cy heterostructures can be found in the Supporting Information.

$$h_{out} = \frac{a_{out}R_{out}^{\ 2}}{r} \tag{3}$$

Here, R_{out} is the radius of the cylindrical jets (R_{out} = 20 μm for this nozzle), r is the distance from the collision point (i.e., distance from the nozzle exit for this geometry), and a_{out} is a scaling factor, which depends on the specific geometry of the nozzle. For this work, we will only consider the sheet centerline, so r will always be parallel to the x axis (Figure 1C). Significantly, this thickness depends only weakly on the velocity of the jets (or equivalently, the liquid flow rate) and is primarily dependent on the nozzle design. Increasing the outer channel liquid flow rate, Q_{out}, increases the total surface area of the liquid sheet and can enable access to larger r and thus smaller h_{out}. Similarly, it was found that liquids with lower air−liquid interfacial tensions (cyclohexane < toluene < water)[32,33] produced larger area sheets with access to smaller h_{out} for the

https://doi.org/10.1021/acs.langmuir.2c01724
Langmuir 2022, 38, 12822−12832

same flow rate, but the scaling factor a_{out} appears to be unchanged.

To produce the liquid heterostructure, a second, immiscible fluid was introduced through the inner channel at a flow rate Q_{in}. Two intermediate flow regimes are apparent before the formation of the stable layered liquid structures. If Q_{in} is below the flow rate, which would produce a stable jet in the absence of the outer fluids (i.e., the nozzle would be periodically dripping, $Q_{in} \lesssim 150$ μL/min for this nozzle), then the resulting sheet was found to appear unstable, where the sheet would reflect diffuse white light instead of specular reflections typical of the stable sheets. As the inner flow rate increased, a more stable structure would form, but the sheets would also contain complicated spanwise wave patterns. These states are shown in Figure 2 for Tol/Wat/Tol heterostructures, in the section labeled "Spanwise Waves."

Just above the flow rate necessary for a stable jet ($Q_{in} \approx 150$ μL/min), a well-formed sheet structure could be produced. However, at some distance from the nozzle, there would be a sudden shift from specular reflection to diffuse white reflection. The front of the stable−unstable transition in the sheet moved further from the nozzle as Q_{in} increases (Figure 2, "Disintegrating"). This process could be analogous to the atomization process, which occurs when a liquid sheet from impinging liquid jets disintegrates at high flow rates into aerosolized droplets.[23,34] A similar behavior was seen in the gas-accelerated liquid sheets at very high gas flow rates as well.[11] As the outer sheet structure is not completely disrupted, it appears that the inner liquid is still confined to the sheet structure. These structures may then allow for the generation of emulsions in liquid sheets, but they were not examined in detail for this work.

At sufficiently high inner flow rates, stable liquid sheets are formed. Representative stable Tol/Wat/Tol and Cy/Wat/Cy heterostructures are shown in Figure 3, with fixed outer fluid flow rate (Q_{out}) and inner fluid flow rate (Q_{in}) increasing from left to right. Two visually distinct morphologies of immiscible liquid heterostructures can be identified. For structures wherein the interfacial tension between the inner and outer fluids is smaller than that between the outer fluid and air, we find that the rims of the two sheets appear to have a similar shape and overlap. That is, the multiliquid sheet will appear as a single sheet structure composed of fully overlapping layers, as can be seen for most of the Tol/Wat/Tol structures (Figure 3, top row) or for sheets generated with water as the outer liquid (see the Supporting Information).

On the other hand, when the interfacial tension between the two fluids significantly exceeds the interfacial tension of the outer fluid with air, then the rims of the inner sheet are not constrained by the rims of the naturally larger outer sheet and will be laterally separated. In this morphology, the inner sheet appears as a smaller sheet with rims fully contained by the larger outer sheet. For the immiscible pairs considered here, this latter case is the most obvious with cyclohexane as the outer fluid and water as the inner fluid (Cy/Wat/Cy heterostructures, Figure 3 bottom) as the interfacial tension of water with cyclohexane (~50 mN/m)[35] is twice that of cyclohexane with air (~25 mN/m).[33] In some cases, multiple leaf-shaped sheet structures are apparent for the center stream, with a second, shorter sheet structure (orthogonal to the first) and then a third sheet (parallel to the first) visible at the highest water flow rate in the Cy/Wat/Cy sheets in Figure 3. At low Q_{in}, the primary inner sheet is observably off-center

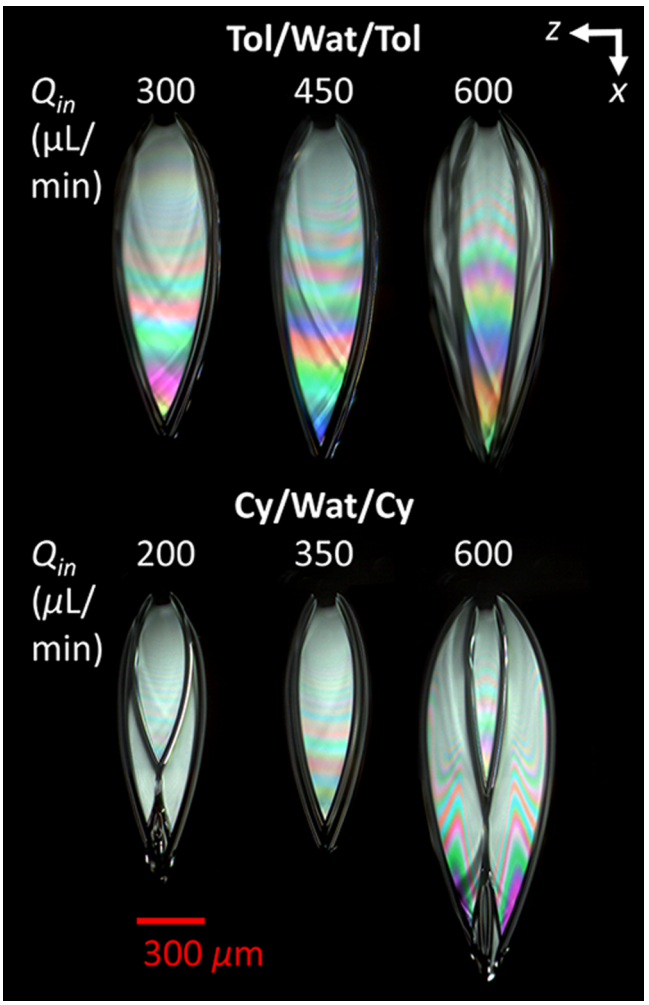

Figure 3. White light images of liquid heterostructure sheets. Shown here are Tol/Wat/Tol (top) and Cy/Wat/Cy (bottom) sheets with an outer flow rate of Q_{out} = 1750 μL/min and a range of inner flow rates, Q_{in}. The sheets display a range of morphologies and thin film interference patterns depending on the flow rate and fluid properties but are all topologically identical to the schematic diagram shown in Figure 1. Additional images can be seen in the Supporting Information.

compared to the outer sheet (Figure 3, bottom left). This asymmetry may be driven by the interfacial tension of the outer sheet as an off-center inner sheet can then have a rim adjacent to the outer sheet's rim. At high Q_{in}, the higher inertia of the inner liquid appears to overcome this effect.

Perhaps the most striking result of this work is that in both of these morphologies, the topology of the liquid heterostructure is the same, with the inner fluid always fully contained by the outer fluid, even in cases wherein multiple inner sheets are formed. Per examination with FTIR microscopy (described in the following section), the outer fluid is always observed to coat the entire inner structure, with fully laterally phase-separated structures never observed. Analogous morphologies are apparent in the secondary, downstream sheet as well (see the Supporting Information), although they appear to reflect diffusely (as in the "Disintegrating" sheets in Figure 2).

We note that it is also possible to use pairs of miscible liquids with this nozzle geometry. Due to the small length scales involved in the liquid sheets, this configuration provides

https://doi.org/10.1021/acs.langmuir.2c01724
Langmuir 2022, 38, 12822−12832

for fast diffusive mixing between two liquids or solutions and allows for the monitoring of, e.g., fast chemical kinetics.[36,37] A full description of this capability will be discussed in a future publication. Similarly, interfacial kinetics could be examined across the immiscible liquid−liquid interfaces, as has been previously examined for the liquid−vapor interfaces in liquid microjets.[38,39]

FTIR Spectromicroscopy. Absorption measurements provide a direct measurement of the amount of material in a given optical path length, which can then be used to determine the thickness of layers comprising a liquid heterostructure. While the common solvents discussed in this work (water, toluene, and cyclohexane) absorb negligibly in the visible spectrum, they have much stronger, spectrally well-separated vibrational transitions in the infrared (IR).[40,41] FTIR microscopy (see the Experimental Materials and Methods section) was then used to examine the spatial distribution of the solvents in the liquid heterostructures.

This method was used to study the composition of the complex morphologies that occur when the interfacial tension between the inner and outer fluids exceeds that between the outer fluid and air. In these cases, the inner layer generally cannot fill the full surface area of the sheet. Looking at the sheet formed by a Cy/Wat/Cy heterostructure, the spatial distribution of the component liquids was determined from the intensity of their characteristic vibrational modes. Figure 4A shows a false-color image of the heterostructure, with red indicating the intensity of a cyclohexane HCH bending mode[42] (~1450 cm^{-1}) and cyan indicating the intensity of the water OH stretch[43] (~3400 cm^{-1}). Spectra taken at two points inside and outside the inner layer sheet are shown in Figure 4B. Water is confined entirely to the smaller-area layer, while cyclohexane is present throughout the entire structure. A similar result was found for all analogous morphologies measured for both Cy/Wat/Cy and Tol/Wat/Tol heterostructures (see the Supporting Information). This measurement provides evidence that the inner layer sheet is entirely surrounded by the outer layer, as opposed to being laterally phase-separated.

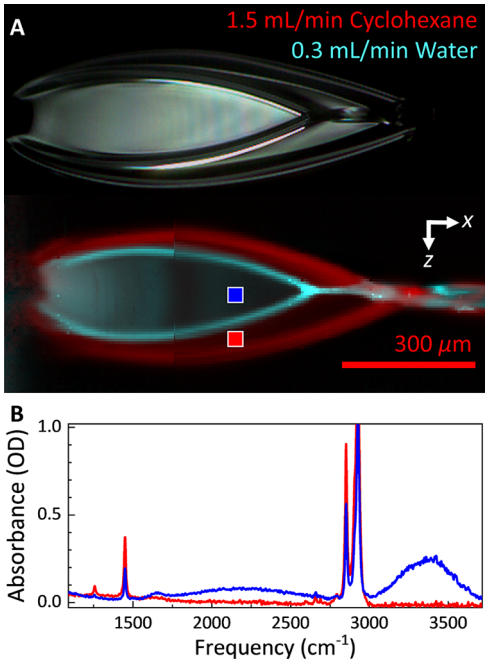

Figure 4. (A) White light image (top) and false-color IR microscopy image (bottom) of a Cy/Wat/Cy heterostructure. (Flow rates: Q_{out} = 1500 μL/min; Q_{in} = 300 μL/min). Red indicates the intensity of a cyclohexane (1450 cm^{-1} IR mode), and blue indicates the intensity of water (3400 cm^{-1} IR mode) in the false color image. Cyclohexane is found throughout the sheet, but water is localized to the smaller interior sheet. (B) Sample FTIR spectra at the points indicated in (A). The sharp cyclohexane peaks are apparent in both, but the broad water peak at 3400 cm^{-1} is only visible in the interior sheet.

The thickness of the inner and outer layers, h_{in} and h_{out}, throughout the sheet was also examined as a function of flow rates. As the sheet flows away from the nozzle, we expect the sheet to get thinner (eq 3), resulting in smaller absorption peaks further from the nozzle (e.g., Figure 5A). The measured absorption intensities could then be converted to thicknesses using eq 1. Sample thickness curves for different inner fluid flow rates, Q_{in}, with constant outer fluid flow rates, Q_{out}, are shown in Figure 5B for Tol/Wat/Tol sheets. The oscillatory behavior in the data arises from imperfect subtraction of the thin film interference background (see the Supporting Information). The absorption measurements show that the inner layer (blue, green, and violet points) also gets progressively thinner with the distance from the nozzle and that the layer thickness at a given distance increases with increasing Q_{in}. Furthest from the nozzle and at low Q_{in}, the inner fluid layer thickness was found to be under 100 nm, with the smallest measured value being just over 30 nm. This thickness is comparable to those found for the ultrathin gas-accelerated sheets produced by the same nozzle.[11] The combined thicknesses of the outer layers (red, yellow, and brown points) were found to fit reasonably well to the theoretical model for a colliding sheet (eq 3, red line in Figure 5B), with a value of a_{out} = 2.9 ± 0.1, and was found to be identical to the single-fluid colliding sheet value for the nozzle and essentially independent of both Q_{in} and Q_{out}, as is typical for a colliding sheet.[21−24] In general, h_{out} could range from ~10 to ~1.5 μm and h_{in} from ~2 μm to 30 nm depending on the position and flow rates.

Notably, the inner sheet thickness, h_{in}, appears to follow roughly the same scaling relationship as the outer layer (eq 3) but with a different scaling factor, a_{in} (i.e., $h_{in} = a_{in}R_{in}^2/r$). Sample lines of best fit to eq 3 are shown in Figure 5B. Unlike the largely invariant behavior of the outer layers, the corresponding values of a_{in} for the inner layers have a dependence on both Q_{in} and Q_{out}. In general, a_{in} increases for an increasing interior flow rate, Q_{in}, and decreases for an increasing outer flow rate, Q_{out}. Plotting the ratio of the inner and outer fluid thicknesses (h_{in}/h_{out}) against the ratio of the inner and outer fluid flow rates (Q_{in}/Q_{out}) suggests conserved behavior across these regimes (Figure 5C). Fitting this master curve to an empirical power law of the form

$$\frac{h_{in}}{h_{out}} = b\left(\frac{Q_{in}}{Q_{out}}\right)^{p} \tag{4}$$

gives values of p = 2.94 ± 0.17 and b = 14.4 ± 3.9 (black line in Figure 5C). However, this relationship does not consider any fluid properties that affect the sheet morphologies and is likely incomplete.

Ellipsometry and Reflectometry. While it is clear from visible and IR microscopy that we can produce stable multiliquid sheets, it is not immediately evident that these structures have well-defined buried liquid−liquid interfaces.

https://doi.org/10.1021/acs.langmuir.2c01724
Langmuir 2022, 38, 12822−12832

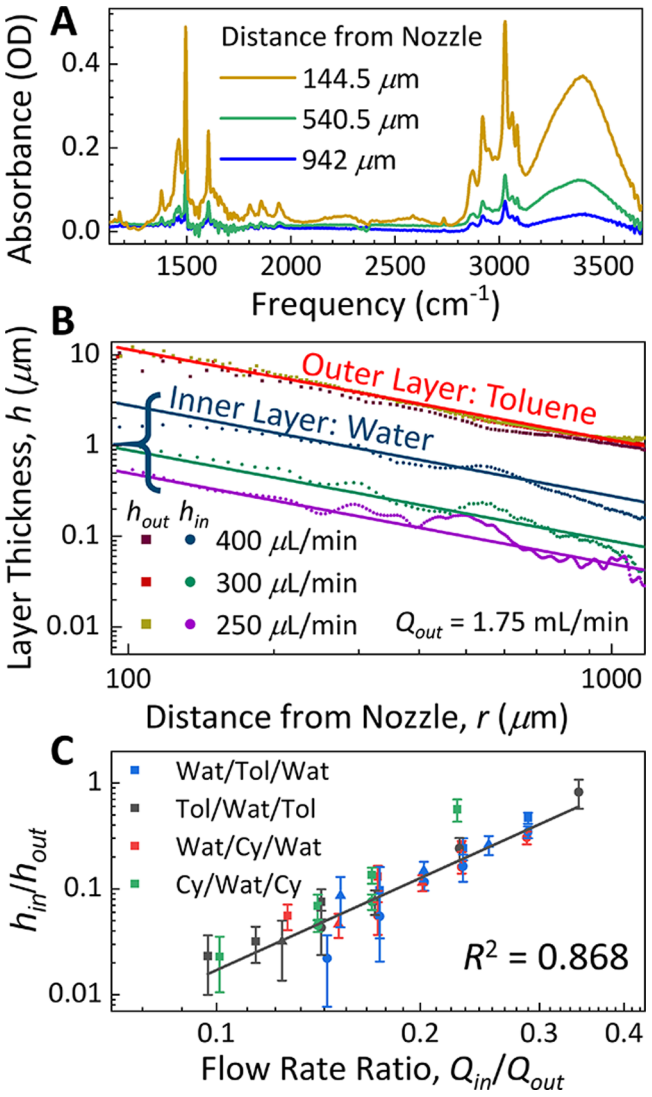

Figure 5. Sample thickness data from FTIR microscopy on the liquid heterostructures. (A) Baseline-subtracted FTIR spectra of a Tol/Wat/Tol heterostructure (Q_{out} = 1750 μL/min; Q_{in} = 300 μL/min) at select distances from the nozzle. As the distance increases, the sheet layers become thinner, causing the toluene modes (sharp peaks) and water mode (broad peak at 3400 cm^{-1}) to decrease in intensity. (B) Layer thicknesses in Tol/Wat/Tol heterostructures with Q_{out} = 1750 μL/min and a range of Q_{in}. The outer layer thicknesses (h_{out}; red, yellow, and brown points) are independent of the flow rates, while the inner layer thicknesses increase with increasing Q_{in} (h_{in}; blue, green, and violet points). All of the layers reasonably follow an $h \approx 1/r$ thickness dependence (eq 3, lines). (C) Ratio of inner to outer layer thicknesses (h_{in}/h_{out}) plotted against the ratio of inner to outer fluid flow rates (Q_{in}/Q_{out}) for the studied heterostructures. Error bars determined from standard errors from fit to eq 3. The black line is a fitted power law with exponent p = 2.94 ± 0.17.

Imaging ellipsometry and reflectometry were employed to interrogate these potential buried interfaces by looking for characteristic optical reflections from them. Generally speaking, if an interface is sharp and flat on the scale of the wavelength of incident photons, then it will appear as an abrupt change in the index of refraction, which allows reflection to occur. If, on the other hand, the interface is smeared out or modulated, then it will be seen as a smooth gradient in the index of refraction and suppress reflections like an antireflective coating.[44] If the experimental reflection intensities from a heterostructure match what is predicted for an ideal layered heterostructure as opposed to a single liquid layer (illustrated in Figure 6A), then this provides strong evidence for well-defined buried liquid−liquid interfaces.

As demonstrated by the IR measurements described in the previous section, the thicknesses of the liquid layers in the heterostructure vary with the distance from the nozzle. The changing thickness profile produces variation in the reflection intensity through thin film interference effects (illustrated in Figure 6B). For the ideal heterostructure shown in Figure 6 (left), there are three main limiting cases for the total reflection, depending on the thicknesses of the component layers. First, all reflections from all four interfaces can fully destructively interfere to give a dark fringe. Second, the reflections from the two inner liquid−liquid interfaces can destructively interfere with each other, in which case the total reflection is solely made up of the reflections from the outer liquid−air interfaces. This case of no interference ("N") between the inner and outer interfaces is indicated with the dotted green line in Figure 6B. The "N" line also corresponds to the reflection intensity for a single fluid sheet without an inner layer (Figure 6B, right). Finally, the reflections from the inner fluid interfaces can constructively interfere with each other and then alternately destructively or constructively interfere with the outer layer reflections ("D" and "C" regions, respectively, in Figure 6B, left). In this case, adjacent bright fringes in the liquid heterostructure will show dramatically different intensities as the changing layer thicknesses cycle the inner and outer reflections in and out of phase.

The intensity maxima of alternating fringes can be used to generate two continuous curves that are 180° out of phase (Figure 6B, left, red and blue dashed curves), which intersect at the "no interference" line. The fringes in the constructive and destructive interference regions have higher and lower reflectivities than the "N" line, respectively. The blue curve switches from constructive interference to destructive interference where it intersects the red curve at the "N" line, with the reverse happening for the red curve.

These characteristic thin film interference patterns can be seen clearly when a heterostructure is imaged using a monochromatic light (see the Experimental Materials and Methods section). Figure 6C demonstrates these patterns with a representative Tol/Wat/Tol heterostructure (Q_{out} = 1750 μL/min, Q_{in} = 300 μL/min) in comparison to a pure water sheet (Q_{out} = 1750 μL/min). Far from the nozzle, the bright fringes in the heterostructure alternate between high and low intensity due to interference between the liquid−air and liquid−liquid interfaces (Figure 6C, red and blue arrows). A similar effect is seen near the nozzle. The presence of these alternating fringes in the interference pattern requires the existence of buried liquid−liquid interfaces in the liquid heterostructure. Between these two regions, in the vicinity of the red and blue curve intersection point, neighboring bright fringes can be seen to have a similar intensity (Figure 6C, green arrow), indicating a region where the inner liquid layer thickness results in destructive interference between the two liquid−liquid interface reflections (and thus no interference with the liquid−air interface reflections). By contrast, the single liquid sheet has uniform fringe brightness (the diagonal dark and bright stripes are from surface imperfections, see the Supporting Information). While the thin film interference pattern indicates the presence of buried liquid−liquid

https://doi.org/10.1021/acs.langmuir.2c01724
Langmuir 2022, 38, 12822−12832

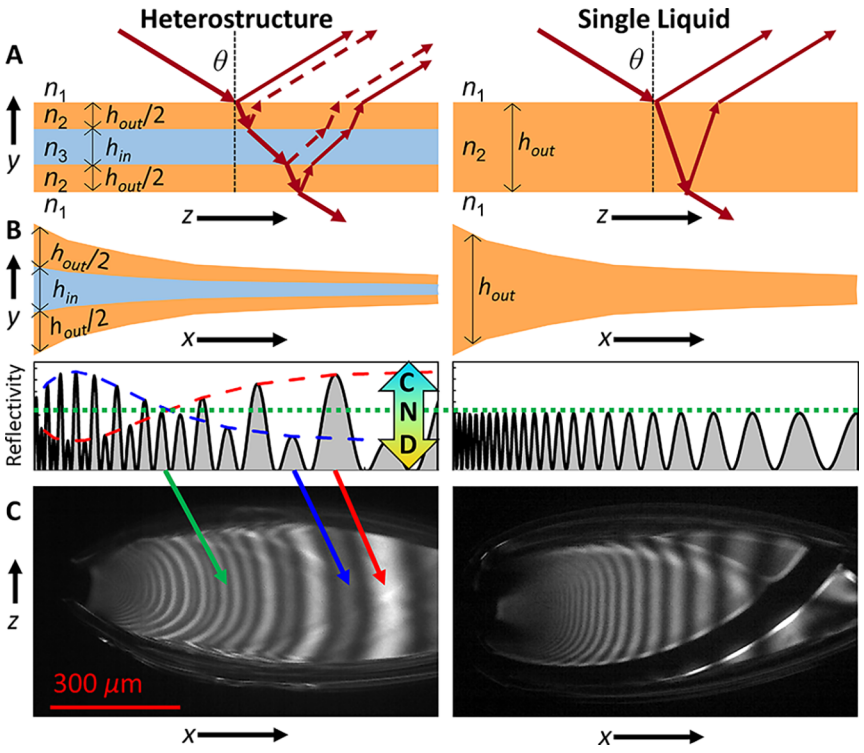

Figure 6. Model of reflection off an ideal liquid heterostructure compared to a single liquid sheet. (A) The reflection intensity depends on thin film interference between the inner and outer layers. (B) Model calculation of how the reflection of a monochromatic light source varies with the distance from the nozzle (r) for a heterostructure and single liquid sheet with a $1/r$ thickness profile. Depending on the thickness of the layers, the reflections from the liquid−liquid interfaces can either not interfere (N), destructively interfere (D), or constructively interfere (C) with the liquid−air interface reflections. The peak intensities of alternating bright fringes in the heterostructure can be used to construct two out-of-phase curves (red and blue dashed lines). The fringes from the single liquid sheet all have their maxima at (N) (green dashed line). (C) Reflection off a Tol/Wat/Tol heterostructure (Q_{out} = 1750 μL/min; Q_{in} = 300 μL/min) and a pure water sheet (Q_{out} = 1750 μL/min) at a θ = 30° AOI using a 630 nm LED. The reflected fringe intensities in the heterostructure show the interference effects illustrated in (B), demonstrating reflections from buried liquid−liquid interfaces. By contrast, the fringes in the pure water sheet are all of equal intensity (diagonal dark and bright stripes are from surface imperfections).

interfaces, imaging ellipsometry was employed to quantitatively analyze the reflections from the liquid heterostructures.

Using the imaging ellipsometer (see the Experimental Materials and Methods section), the ellipsometric angles, Ψ and Δ, can be mapped across a liquid heterostructure at a range of AOIs, θ. As was shown in Figure 6C, the intensity of reflection from the heterostructure is modulated by interference between the liquid−liquid and air−liquid interfaces. This effect produces similar modulations in the ellipsometric observables. One phenomenon directly indicative of buried liquid−liquid interfaces can be seen in the phase difference (Δ) between the s and p reflection components. A map of Δ across the representative Tol/Wat/Tol heterostructure at a selection of θ can be seen in Figure 7. In general, the liquid sheets act as near-ideal dielectric layers at 630 nm, where the total phase shift is 0° for the s polarization and switches from 180° to 0° at Brewster's angle for the p polarization. However, the precise value of Brewster's angle for the heterostructure depends on the thickness of the inner liquid layer. At angles of incidence less than Brewster's angle for both component liquids, Δ is 180° across the sheet, and above Brewster's angle for both liquids, Δ is 0° (Figure 7, top and bottom, respectively). However, between the two liquid Brewster's angles, alternating fringes in the sheet will reflect with the alternating phase (Figure 7, middle). This phase modulation is an additional striking demonstration of the buried liquid−liquid interfaces in the liquid heterostructures.

A similar modulation is apparent in the measurement of Ψ at most θ but is most easily measured at large θ wherein both the C and D bands have high reflectivities (although the large angle and finite depth of field of the objective distort the edges of the sheet). In general, the reflection modulation demonstrated in Figure 6C will be different between the s and p polarization components, resulting in a modulation of the reflected polarization angle (corresponding to the ellipsometric angle $\tan \Psi = |r_p|/|r_s|$). A map of Ψ across a liquid heterostructure (the Tol/Wat/Tol structure examined in Figure 6C) at a θ = 70° angle of incidence is shown in Figure 8A, where cyan indicates a low value of Ψ and yellow indicates a high value of Ψ. For most of the heterostructure, the angle of the reflected polarization alternates between high and low values as neighboring bands produce alternating constructive or destructive interference between the outer and inner layers. This polarization modulation is once again clear evidence of sharp buried liquid−liquid interfaces within the sheet, which can be modeled to determine the layer dimensions.

Combining Absorption and Reflection Measurements. A full description of the liquid heterostructure can now be obtained by combining the reflection and absorbance measurements. Using the ellipsometry results in Figure 8, layer thicknesses can be determined if a model structure is adopted (e.g., Figure 6A). Complementarily, the absorption measurements from the FTIR microscopy provide information on the total amount of each liquid at every point in the sheet but

https://doi.org/10.1021/acs.langmuir.2c01724
Langmuir 2022, 38, 12822−12832

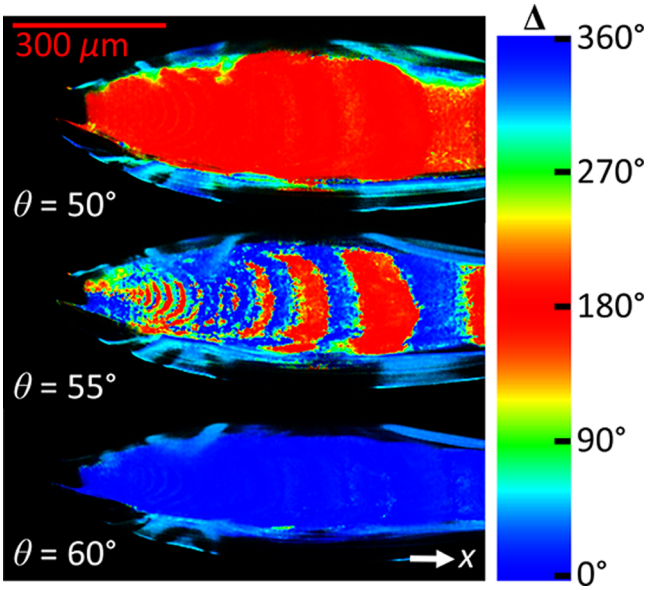

Figure 7. Map of phase difference Δ between the *s* and *p* reflection components for different angles of incidence, θ, in a Tol/Wat/Tol heterostructure. (Flow rates: Q_{out} = 1750 μL/min; Q_{in} = 300 μL/min). If the angle of incidence is less than (top image) or greater than (bottom image) Brewster's angle for both component liquids, then Δ is uniformly 180 or 0°, respectively. Between the two component liquids' Brewster's angles (middle image), Δ can flip 180° between adjacent fringes due to interference effects.

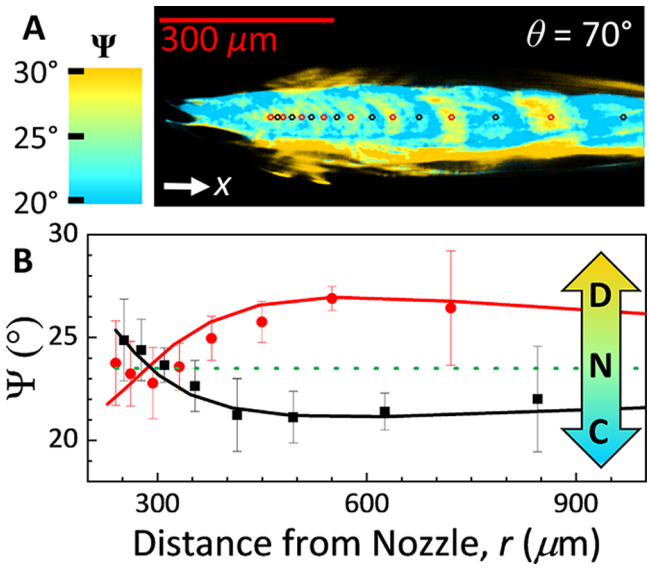

Figure 8. (A) Map of ellipsometric angle Ψ at a θ = 70° AOI for a Tol/Wat/Tol heterostructure. (Flow rates: Q_{out} = 1750 μL/min; Q_{in} = 300 μL/min). Constructive (C) and destructive (D) interference between reflections from the liquid/liquid and liquid/air interfaces result in alternating fringes of high and low Ψ. (B) Comparison of measured and calculated values of Ψ using the ideal heterostructure model (points and curves, respectively). Ψ was measured at fringe intensity maxima to get the best signal to noise (points indicated in (A)). Fringes are split into alternating pairs (red and black) corresponding to a 180° phase shift between the inner and outer reflections (analogous to the red and blue curves in Figure 6B). Calculated values were derived from the liquid layer thicknesses measured by IR (Figure 5B) using the ideal heterostructure model (Figure 6). Measured values are within error of the calculated values at all points (error bars from standard deviation of Ψ in the selected region). The dashed green line is the predicted value of Ψ for a uniform toluene sheet (N − no interference).

cannot be used to distinguish any particular structure. If the calculated layer thicknesses from the two methods correspond well with the amount of material in each point, then this strongly supports the model heterostructure used for the reflection studies. The thicknesses of the layers were determined using the fits of the IR data to eq 3 (lines in Figure 5B), with manual fine adjustment to the *a* parameters to better align to the observed locations of the bright fringes in the thin film interference pattern (a_{out} = 2.99 and a_{in} = 0.96, within error of the purely IR determined values of a_{out} = 2.9 ± 0.1 and a_{in} = 0.9 ± 0.2). For simplicity, it was assumed that the outer toluene layers were of equal thickness ($h_{out}/2$) based on the symmetry of the nozzle. Ψ can then be calculated with the transfer matrix method[27,28] (see the Supporting Information) for each point in the sheet using these layer thicknesses and the liquid indices of refraction.

The measurements of Ψ are compared quantitatively with theory in Figure 8B, where the points are the measured values at the peaks of the bright fringes, corresponding to the overlaid dots in Figure 8A. Theoretical calculations for the model heterostructure using the IR-determined thicknesses are shown as solid curves in Figure 8B. The changing layer thicknesses cycle the inner and outer reflections in and out of phase, which results in fringes with alternating values of Ψ. As was seen with the reflected fringe intensities in Figure 6B, these sets of alternating fringes can be used to construct two branches, which are 180° out of phase with each other (Figure 8B, red and black curves). As in Figure 6B, the curves shown in Figure 8B describe the calculated value of Ψ for fully constructive interference between the outer liquid−air interface reflections (i.e., interference fringe maxima, see the Supporting Information), which is then modulated by interference from the inner layer reflections. This branching behavior is a direct result of the buried interfaces and is not seen for single-fluid sheets, as indicated by the dashed line of constant Ψ in Figure 8B calculated for a single-fluid toluene sheet.

These calculated values were compared to the measured values of Ψ around the most intense point of each bright fringe, which yield the highest signal to noise (Figure 8A, red and black dots for the sets of alternating fringes). At all points, the measured values of Ψ for each fringe were within experimental error of the ideal heterostructure values (Figure 8B), which corresponds to most of the sheet containing a water layer between 300 and 100 nm thick. Both sets of fringes also demonstrate the predicted pattern, wherein they start near the "No Interference" (N) value 300 μm from the nozzle (predicted value for a single-fluid toluene sheet, dashed line in Figure 8B) and show greater deviations at a greater distance from the nozzle. The representative Tol/Wat/Tol heterostructure is then quantitatively consistent with an ideal heterostructure with layer thicknesses corresponding to the values determined with the IR microscopy measurements. The experimentally determined cross section for the example Tol/Wat/Tol heterostructure is shown in Figure 9A, where the solid curves are the fit values used for the ellipsometry calculation shown in Figure 8B and the points are the thicknesses determined from IR microscopy shown in Figure 5. As a final validation of this determined structure, the colored fringes seen in the white light reflection images (e.g., Figure 3) can be predicted from the profile shown in Figure 9A using the

https://doi.org/10.1021/acs.langmuir.2c01724
Langmuir 2022, 38, 12822−12832

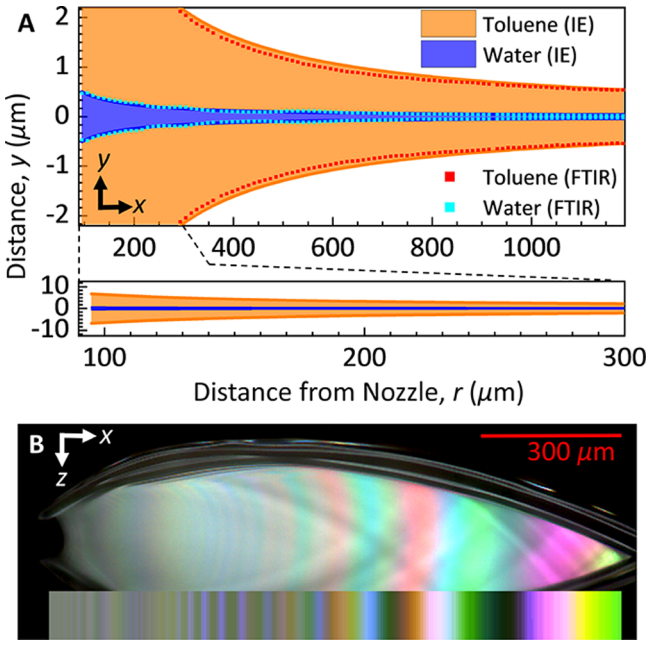

Figure 9. (A) Thickness profile for the Tol/Wat/Tol heterostructure (Q_{out} = 1750 μL/min; Q_{in} = 300 μL/min) from the ellipsometric model (solid curves) and FTIR absorbance (points). The two methods provide a common picture of the liquid heterostructure dimensions. Bottom: the thickest part of the sheet with equal scaling of the *x* and *y* axes, illustrating the flatness of the sheet. (B) True-color white light image of the heterostructure compared to calculated white light reflection for an idealized heterostructure using the profile from (A). The good agreement between colored bands provides additional validation for the cross-sectional profile.

transfer matrix method, the white light LED spectrum, and the wavelength-dependent indices of refraction (see the Supporting Information). While it is challenging to perfectly reproduce the camera's color and exposure settings, the calculated band colors provide a good quality match to the sheet's observed fringe colors (Figure 9B). The combined white light reflection, ellipsometry measurements, and IR microscopy measurements then provide a consistent picture of a near-ideal liquid heterostructure containing optically flat and sharp liquid–liquid interfaces.

CONCLUSIONS

This work demonstrated the generation of liquid heterostructures, free-flowing laminar structures containing well-defined thin layers of immiscible liquids. Absorption measurements from FTIR microscopy demonstrated that the inner layer can be just tens of nanometers thick and follows thickness scaling relationships similar to those seen for single-fluid colliding sheets and gas-accelerated sheets. Reflectivity and ellipsometry measurements demonstrated reflections off buried liquid–liquid interfaces, which indicate optically sharp and smooth interfaces. Excellent correspondence was found between the layer thicknesses determined by absorption measurements to those determined by reflectivity and ellipsometric measurements. These results indicate that the liquid heterostructures formed are essentially ideal and contain sharp, large-area, liquid–liquid interfaces.

As the inner layer can be tuned to be only tens of nanometers thick, liquid heterostructures are ideal spectroscopic targets for interface studies as the amount of bulk liquid not involved with the interface is greatly reduced. The free-flowing nature of the heterostructure also provides a number of unique benefits. Sheet jets at comparable flow rates have been used successfully for liquid studies in vacuum by employing high-performance vacuum pumps and liquid catching systems,[7−9,13,45] which allows liquid–liquid interfaces to be studied with techniques that have been previously inaccessible due to the challenges of maintaining liquids in vacuum. The liquid interface is also constantly refreshed, which allows for examination of kinetics of interface formation as well as chemical and physical processes and reactions mediated by the interface on fast time scales (ca. 100 μs, based on the jet velocity and sheet length). This unique collection of attributes should make the liquid heterostructure sheet jets a powerful tool for examining the liquid–liquid interface.

ASSOCIATED CONTENT

Supporting Information

The Supporting Information is available free of charge at https://pubs.acs.org/doi/10.1021/acs.langmuir.2c01724.

Description of surface imperfections on the liquid sheets, description and images of water/hydrocarbon/water heterostructures, images of the Cy/Wat/Cy stable/unstable transition, additional FTIR microscopy images of heterostructures, description of thin film interference calculations, description of ellipsometry methods, description of the microfluidic nozzle, and description of secondary sheets (PDF)

AUTHOR INFORMATION

Corresponding Author

Jake D. Koralek − *Linac Coherent Light Source, SLAC National Accelerator Laboratory, Menlo Park, California 94025, United States*; Email: koralek@slac.stanford.edu

Authors

David J. Hoffman − *Linac Coherent Light Source, SLAC National Accelerator Laboratory, Menlo Park, California 94025, United States*; orcid.org/0000-0001-8518-7676

Hans A. Bechtel − *Advanced Light Source, Lawrence Berkeley National Laboratory, Berkeley, California 94720, United States*

Diego A. Huyke − *Department of Mechanical Engineering, Stanford University, Stanford, California 94305, United States*; orcid.org/0000-0002-8335-6613

Juan G. Santiago − *Department of Mechanical Engineering, Stanford University, Stanford, California 94305, United States*; orcid.org/0000-0001-8652-5411

Daniel P. DePonte − *Linac Coherent Light Source, SLAC National Accelerator Laboratory, Menlo Park, California 94025, United States*

Complete contact information is available at: https://pubs.acs.org/10.1021/acs.langmuir.2c01724

Notes

The authors declare no competing financial interest.

ACKNOWLEDGMENTS

This work was supported by the Department of Energy, Laboratory Directed Research and development program at SLAC National Accelerator Laboratory, under contract DE-AC02-76SF00515. Use of the Linac Coherent Light Source

(LCLS) biolabs, SLAC National Accelerator Laboratory, is supported by the U.S. Department of Energy, Office of Science, Office of Basic Energy Sciences under Contract No. DE-AC02-76SF00515. FTIR spectromicroscopy experiments were performed at the Advanced Light Source, a U.S. DOE Office of Science User Facility under contract no. DE-AC02-05CH11231. D.A.H. was supported by a National Science Foundation Graduate Research Fellowship. We thank R. J. Saykally for helpful comments which improved this manuscript.

REFERENCES

(1) Piradashvili, K.; Alexandrino, E. M.; Wurm, F. R.; Landfester, K. Reactions and Polymerizations at the Liquid−Liquid Interface. *Chem. Rev.* **2016**, *116*, 2141−2169.
(2) Benjamin, I. Molecular Structure and Dynamics at Liquid-Liquid Interfaces. *Annu. Rev. Phys. Chem.* **1997**, *48*, 407−451.
(3) Booth, S. G.; Dryfe, R. A. W. Assembly of Nanoscale Objects at the Liquid/Liquid Interface. *J. Phys. Chem. C* **2015**, *119*, 23295−23309.
(4) Benjamin, l. Mechanism and Dynamics of Ion Transfer Across a Liquid-Liquid Interface. *Science* **1993**, *261*, 1558−1560.
(5) Eisenthal, K. B. Equilibrium and Dynamic Processes at Interfaces by Second Harmonic and Sum Frequency Generation. *Annu. Rev. Phys. Chem.* **1992**, *43*, 627−661.
(6) Perera, J. M.; Stevens, G. W. Spectroscopic studies of molecular interaction at the liquid−liquid interface. *Anal. Bioanal. Chem.* **2009**, *395*, 1019−1032.
(7) Ekimova, M.; Quevedo, W.; Faubel, M.; Wernet, P.; Nibbering, E. T. J. A liquid flatjet system for solution phase soft-x-ray spectroscopy. *Struct. Dyn.* **2015**, *2*, No. 054301.
(8) Galinis, G.; Strucka, J.; Barnard, J. C. T.; Braun, A.; Smith, R. A.; Marangos, J. P. Micrometer-thickness liquid sheet jets flowing in vacuum. *Rev. Sci. Instrum.* **2017**, *88*, No. 083117.
(9) Fondell, M.; Eckert, S.; Jay, R. M.; Weniger, C.; Quevedo, W.; Niskanen, J.; Kennedy, B.; Sorgenfrei, F.; Schick, D.; Giangrisostomi, E.; Ovsyannikov, R.; Adamczyk, K.; Huse, N.; Wernet, P.; Mitzner, R.; Föhlisch, A. Time-resolved soft X-ray absorption spectroscopy in transmission mode on liquids at MHz repetition rates. *Struct. Dyn.* **2017**, *4*, No. 054902.
(10) Smith, J. W.; Saykally, R. J. Soft x-ray absorption spectroscopy of liquids and solutions. *Chem. Rev.* **2017**, *117*, 13909−13934.
(11) Koralek, J. D.; Kim, J. B.; Brůža, P.; Curry, C. B.; Chen, Z.; Bechtel, H. A.; Cordones, A. A.; Sperling, P.; Toleikis, S.; Kern, J. F.; Moeller, S. P.; Glenzer, S. H.; DePonte, D. P. Generation and characterization of ultrathin free-flowing liquid sheets. *Nat. Commun.* **2018**, *9*, 1353.
(12) Ha, B.; DePonte, D. P.; Santiago, J. G. Device design and flow scaling for liquid sheet jets. *Phys. Rev. Fluids* **2018**, *3*, No. 114202.
(13) Menzi, S.; Knopp, G.; Al Haddad, A.; Augustin, S.; Borca, C.; Gashi, D.; Huthwelker, T.; James, D.; Jin, J.; Pamfilidis, G.; Schnorr, K.; Sun, Z.; Wetter, R.; Zhang, Q.; Cirelli, C. Generation and simple characterization of flat, liquid jets. *Rev. Sci. Instrum.* **2020**, *91*, 105109.
(14) Nunes, J. P. F.; Ledbetter, K.; Lin, M.; Kozina, M.; DePonte, D. P.; Biasin, E.; Centurion, M.; Crissman, C. J.; Dunning, M.; Guillet, S.; Jobe, K.; Liu, Y.; Mo, M.; Shen, X.; Sublett, R.; Weathersby, S.; Yoneda, C.; Wolf, T. J. A.; Yang, J.; Cordones, A. A.; Wang, X. J. Liquid-phase mega-electron-volt ultrafast electron diffraction. *Struct. Dyn.* **2020**, *7*, No. 024301.
(15) Yang, J.; Dettori, R.; Nunes, J. P. F.; List, N. H.; Biasin, E.; Centurion, M.; Chen, Z.; Cordones, A. A.; Deponte, D. P.; Heinz, T. F.; Kozina, M. E.; Ledbetter, K.; Lin, M.-F.; Lindenberg, A. M.; Mo, M.; Nilsson, A.; Shen, X.; Wolf, T. J. A.; Donadio, D.; Gaffney, K. J.; Martinez, T. J.; Wang, X. Direct observation of ultrafast hydrogen bond strengthening in liquid water. *Nature* **2021**, *596*, 531−535.
(16) George, K. M.; Morrison, J. T.; Feister, S.; Ngirmang, G. K.; Smith, J. R.; Klim, A. J.; Snyder, J.; Austin, D.; Erbsen, W.; Frische, K. D.; Nees, J.; Orban, C.; Chowdhury, E. A.; Roquemore, W. M. High-repetition-rate (>kHz) targets and optics from liquid microjets for high-intensity laser−plasma interactions. *High Power Laser Sci. Eng.* **2019**, *7*, No. e50.
(17) Yin, Z.; Luu, T. T.; Wörner, H. J. Few-cycle high-harmonic generation in liquids: in-operando thickness measurement of flat microjets. *J. Phys. Photonics* **2020**, *2*, No. 044007.
(18) Obst, L.; Göde, S.; Rehwald, M.; Brack, F.-E.; Branco, J.; Bock, S.; Bussmann, M.; Cowan, T. E.; Curry, C. B.; Fiuza, F.; Gauthier, M.; Gebhardt, R.; Helbig, U.; Huebl, A.; Hübner, U.; Irman, A.; Kazak, L.; Kim, J. B.; Kluge, T.; Kraft, S.; Loeser, M.; Metzkes, J.; Mishra, R.; Rödel, C.; Schlenvoigt, H.-P.; Siebold, M.; Tiggesbäumker, J.; Wolter, S.; Ziegler, T.; Schramm, U.; Glenzer, S. H.; Zeil, K. Efficient laser-driven proton acceleration from cylindrical and planar cryogenic hydrogen jets. *Sci. Rep.* **2017**, *7*, 10248.
(19) Atencia, J.; Beebe, D. J. Controlled microfluidic interfaces. *Nature* **2005**, *437*, 648−655.
(20) Ismagilov, R. F.; Stroock, A. D.; Kenis, P. J. A.; Whitesides, G.; Stone, H. A. Experimental and theoretical scaling laws for transverse diffusive broadening in two-phase laminar flows in microchannels. *Appl. Phys. Lett.* **2000**, *76*, 2376−2378.
(21) Taylor, G. I. Formation of thin flat sheets of water. *Proc. R. Soc. Lond. A* **1960**, *259*, 1−17.
(22) Choo, Y. J.; Kang, B. S. Parametric study on impinging-jet liquid sheet thickness distribution using an interferometric method. *Exp. Fluids* **2001**, *31*, 56−62.
(23) Bush, J. W. M.; Hasha, A. E. On the collision of laminar jets: fluid chains and fishbones. *J. Fluid Mech.* **2004**, *511*, 285−310.
(24) Hasson, D.; Peck, R. E. Thickness distribution in a sheet formed by impinging jets. *AIChE J.* **1964**, *10*, 752−754.
(25) Kozma, I. Z.; Krok, P.; Riedle, E. Direct measurement of the group-velocity mismatch and derivation of the refractive-index dispersion for a variety of solvents in the ultraviolet. *J. Opt. Soc. Am. B* **2005**, *22*, 1479.
(26) Daimon, M.; Masumura, A. Measurement of the refractive index of distilled water from the near-infrared region to the ultraviolet region. *Appl. Opt.* **2007**, *46*, 3811.
(27) Harbecke, B. Coherent and incoherent reflection and transmission of multilayer structures. *Appl. Phys. B: Lasers Opt.* **1986**, *39*, 165−170.
(28) Byrnes, S. J.Multilayer optical calculations. *arXiv [Preprint]* **2016**.
(29) Tompkins, H.; Irene, E. A., *Handbook of ellipsometry*. William Andrew: 2005.
(30) Asinovski, L.; Beaglehole, D.; Clarkson, M. T. Imaging ellipsometry: quantitative analysis. *Phys. Status Solidi A* **2008**, *205*, 764−771.
(31) Chou, C.; Teng, H.-K.; Yu, C.-J.; Huang, H.-S. Polarization modulation imaging ellipsometry for thin film thickness measurement. *Opt. Commun.* **2007**, *273*, 74−83.
(32) Lange, N. A.; Dean, J. A., *Lange's Handbook of Chemistry*. McGraw-Hill: 1973.
(33) Korosi, G.; Kovats, E. S. Density and surface tension of 83 organic liquids. *J. Chem. Eng. Data* **1981**, *26*, 323−332.
(34) Ryan, H. M.; Anderson, W. E.; Pal, S.; Santoro, R. J. Atomization characteristics of impinging liquid jets. *J. Propul. Power* **1995**, *11*, 135−145.
(35) Backes, H. M.; Jing Jun, M.; Bender, E.; Maurer, G. Interfacial tensions in binary and ternary liquid—liquid systems. *Chem. Eng. Sci.* **1990**, *45*, 275−286.
(36) Schewe, H. C.; Credidio, B.; Ghrist, A. M.; Malerz, S.; Ozga, C.; Knie, A.; Haak, H.; Meijer, G.; Winter, B.; Osterwalder, A. Imaging of chemical kinetics at the water-water interface in a free-flowing liquid flat-jet. *J. Am. Chem. Soc.* **2022**, *144*, 7790−7795.
(37) Erni, P.; Elabbadi, A. Free Impinging Jet Microreactors: Controlling Reactive Flows via Surface Tension and Fluid Viscoelasticity. *Langmuir* **2013**, *29*, 7812−7824.
(38) Castro, A.; Ong, S.; Eisenthal, K. B. Studies of molecular properties at the surface of a liquid jet by second harmonic generation. *Chem. Phys. Lett.* **1989**, *163*, 412−416.

https://doi.org/10.1021/acs.langmuir.2c01724
Langmuir 2022, 38, 12822−12832

(39) Hutchison, J.; Klenerman, D.; Manning-Benson, S.; Bain, C. Measurements of the Adsorption Kinetics of a Cationic Surfactant in a Liquid Jet by Ellipsometry. *Langmuir* **1999**, *15*, 7530−7533.
(40) Hale, G. M.; Querry, M. R. Optical Constants of Water in the 200-nm to 200-μm Wavelength Region. *Appl. Opt.* **1973**, *12*, 555.
(41) Myers, T. L.; Tonkyn, R. G.; Danby, T. O.; Taubman, M. S.; Bernacki, B. E.; Birnbaum, J. C.; Sharpe, S. W.; Johnson, T. J. Accurate Measurement of the Optical Constants n and k for a Series of 57 Inorganic and Organic Liquids for Optical Modeling and Detection. *Appl. Spectrosc.* **2018**, *72*, 535−550.
(42) Takahashi, H.; Shimanouchi, T.; Fukushima, K.; Miyazawa, T. Infrared spectrum and normal vibrations of cyclohexane. *J. Mol. Spectrosc.* **1964**, *13*, 43−56.
(43) Venyaminov, S. Y.; Prendergast, F. G. Water (H2O and D2O) Molar Absorptivity in the 1000−4000 cm−1 Range and Quantitative Infrared Spectroscopy of Aqueous Solutions. *Anal. Biochem.* **1997**, *248*, 234−245.
(44) Minot, M. J. The angluar reflectance of single-layer gradient refractive-index films. *J. Opt. Soc. Am.* **1977**, *67*, 1046.
(45) Crissman, C. J.; Mo, M.; Chen, Z.; Yang, J.; Huyke, D. A.; Glenzer, S. H.; Ledbetter, K.; Nunes, J. P. F.; Ng, M. L.; Wang, H.; Shen, X.; Wang, X.; DePonte, D. P. Sub-micron thick liquid sheets produced by isotropically etched glass nozzles. *Lab Chip* **2022**, *22*, 1365−1373.

https://doi.org/10.1021/acs.langmuir.2c01724
Langmuir 2022, 38, 12822−12832